

CHEMICAL PHYSICS

Substantially improved efficiency and selectivity of carbon dioxide reduction by superior hydrated electron in microdroplet

Qiuyue Ge¹†, Yangyang Liu^{1,2}†, Wenbo You¹, Yumo Li³, Wei Wang¹, Le Yang¹, Lifang Xie¹, Kejian Li¹, Licheng Wang¹, Minglu Ma¹, Runbo Wang¹, Jilun Wang¹, Tingting Huang¹, Tao Wang¹, Xuejun Ruan¹, Minbiao Ji³, Liwu Zhang^{1,4,5}*

The photochemical conversion of CO_2 into valuable fuels faces challenges of low efficiency and poor selectivity. Hydrated electrons (e_{aq}^{-}), with their extremely negative reduction potential, are promising CO_2 -reducing agents, yet their short lifetime limits selectivity and high-energy-density product formation. Herein, we show that microdroplet interfaces with strong electric fields (10^9 volts per meter) substantially extend the lifespan of e_{aq}^{-} generated from industrial sulfite pollutants (SO_3^{2-}), lowering energy barriers in the CO_2 reduction reaction and enabling targeted product formation. The machine learning strategy identified microdroplet size as the key parameter controlling electric field strength, product yield, and selectivity. In our lab-based scaled-up system, microdroplets <10 micrometers improved performance by four to seven orders of magnitude over bulk-phase systems, achieving ~99% methanol selectivity. Strong interfacial electric fields stabilize intermediates and modulate carbon-oxygen bond lengths, directing pathways to high-value products. This approach enables sustainable CO_2 utilization via microdroplets, potentially producing fuels from waste.

Copyright © 2025 The Authors, some rights reserved; exclusive licensee American Association for the Advancement of Science. No claim to original U.S.
Government Works.
Distributed under a Creative Commons Attribution
NonCommercial

INTRODUCTION

Over the past few decades, the solar-driven photochemistry conversion of greenhouse carbon dioxide (CO₂) into hydrocarbon fuels [methanol (CH₃OH), formic acid (HCOOH), etc.] has emerged as a promising strategy to meet global energy demands while mitigating climate change (1). For the photochemical CO₂ reduction, the hydrated electron (e_{aq}⁻), distinguished by its exceptionally negative standard reduction potential of -2.9 V, has been acclaimed as one of the most potential agents for photochemical reduction (2). Its applications extend beyond CO₂ reduction to include the decomposition of persistent halogenated pollutants and versatile chemical synthesis (3). In aqueous environments, the rapid interaction between e_{aq}^{-} and CO_2 generates the $CO_2^{\bullet -}$ anion with a remarkably high reaction rate constant of $\sim 10^{10} \, \mathrm{M}^{-1} \, \mathrm{s}^{-1}$ at room temperature (4). e_{aq}^{-} can be generated as $e_{aq}^{\bullet -}$ can be generated as $e_{aq}^{\bullet -}$ ated using semiconductor catalysts, such as diamond, which enables the injection of electrons into the surrounding liquid environment when the conduction band position exceeds the thermodynamic potential of the liquid's molecular constituents (5).

Recent studies have identified SO_3^{2-} as a viable source of e_{aq}^{-} source for inorganic carbon reduction, yielding organic molecules critical to the origins of life (6). Notably, the SO_3^{2-} anions, derived from the caustic liquid adsorption of a large quantity of SO_2 flue gas emitted from power plants, vehicles, and factories, exhibit a high quantum yield (0.11 to 0.17 mol/E) $(SO_3^{2-} + h\nu \rightarrow SO_3^{-} + e^{-})$ (7),

thus essentially providing numerous e_{aq}^{-} through electron photodetachment for industrial CO_2 reduction. Although e_{aq}^{-} is a powerful reductant capable of efficiently reacting with environmentally substantial contaminants, its inherently short lifetime limits its utility in traditional bulk-phase, solar-driven processes. On the other hand, conventional CO_2 reduction by e_{aq}^{-} typically requires substantial energy inputs for producing e_{aq}^{-} , such as exposure to high-energy rays (8) or temperatures (9). Moreover, e_{aq}^{-} -mediated photochemical CO_2 reduction suffers from low selectivity and the inability to specifically produce high-energy-density products, which substantially limits the practical applications of e_{aq}^{-} in CO_2 reduction (10).

Microdroplets, which are believed to be featured in a unique aqueous environment and have abundant gas-liquid interfaces (11), show abnormal physical-chemical properties, particularly strong interfacial electric fields, that can markedly accelerate reactions compared to bulk-phase reactions and even produce products that cannot be synthesized in the bulk aqueous medium (7, 12, 13). Early studies suggest that the spontaneous donation of electrons by OH $^-$ in water microdroplets is responsible for the hydrogenation of CO $_2$ to HCOOH or other species, which are potentially driven by strong electric fields at or near the interfaces of water microdroplets. Nevertheless, the yields are commonly low (14), and there is a lack of research on directing the production of specific products. Yet so far, to our best knowledge, how interfacial $e_{\rm aq}^-$ functionalizes in microdroplets remains an open question (15), and rare information is currently available for the reduction of CO $_2$ by hydrated electrons in microdroplets.

Here, we demonstrate that high efficiency and selectivity in CO_2 reduction can be achieved using hydrated electrons (e_{aq}^{-}) generated from industrial waste–derived SO_3^{2-} at the gas-liquid interface of microdroplets. By integrating machine learning, advanced microdroplet-generating devices, and optical imaging techniques, we quantified substantial enhancement factors in CO_2 reduction across a wide range of microdroplet sizes and interfacial electric field strengths. Our results reveal that interfacial electric fields within microdroplets,

¹Department of Environmental Science and Engineering, Fudan University, Shanghai 200433, People's Republic of China. ²Department of Civil and Environmental Engineering, Virginia Tech, Blacksburg, VA 24061, USA. ³State Key Laboratory of Surface Physics and Department of Physics, Fudan University, Shanghai 200092, People's Republic of China. ⁴Shanghai Key Laboratory of Atmospheric Particle Pollution and Prevention, Fudan University, Shanghai 200433, People's Republic of China. ⁵Shanghai Institute of Pollution Control and Ecological Security, Shanghai 200092, People's Republic of China.

^{*}Corresponding author. Email: zhanglw@fudan.edu.cn

[†]These authors contributed equally to this work.

reaching intensities of up to $10^9~V~m^{-1}$, are pivotal in enhancing both the efficiency and selectivity of CO_2 reduction. This electrostatic environment extends the lifetime of $\mathrm{e}_{\mathrm{aq}}^-$ and reduces energy barriers at critical stages of the CO_2 reduction reaction ($\mathrm{CO}_2\mathrm{RR}$). These findings position microdroplets as efficient photochemical reaction chambers for $\mathrm{e}_{\mathrm{aq}}^-$ -mediated multielectron reactions, markedly improving the yield and selectivity of $\mathrm{CO}_2\mathrm{RR}$ products as the microdroplet size decreases. This work provides a strategy for developing highly efficient CO_2 utilization strategies and producing value-added C—H fuels, offering a transformative approach to address the energy crisis and climate change.

RESULTS

Substantially accelerated photochemical ${\rm CO_2RRs}$ in the PMEF system

We applied a photochemical microdroplet reaction system (hereafter denoted as the PMEF system) by producing sprayed microdroplets of strong interfacial electric field (on the order of 10⁹ V m⁻¹, characterized and discussed in the later section) on the hydrophobic substrate, followed by the subsequent reaction in a custom-designed flow-cell reactor upon light irradiation (Fig. 1A and fig. S1). The relative humidity (RH) in the reactor's headspace was maintained at ~90% for all experiments, which ensures the microdroplet stability throughout the process, as evidenced by the bright-field images captured in some trials where there is a marginal change in size dimension throughout the reaction (fig. S2). We selected HCOOH as the target product to evaluate the reductive performance differences of hydrated electrons (e_{aq}⁻) between microdroplet and bulk-phase

environments, considering that HCOOH is the primary detectable product in both the 300-µm microdroplet and 3-ml bulk-phase systems. In the PMEF system, the HCOOH concentration increased over time, reaching 22.2 mM (microdroplet size, ~300 μm) after 3 hours of irradiation—far exceeding the 2.3 mM observed in the bulk phase (Fig. 1B). Increasing the initial concentration of inorganic carbon sources (CO2 or NaHCO3) further boosted HCOOH yields (Fig. 1, C and D). CO₂ reduction efficiency strongly correlated with light intensity in both the PMEF and bulk systems, confirming the photochemical basis of HCOOH formation. Notably, at a low intensity of 0.77 mW/cm², the PMEF system outperformed the bulk phase by one or two orders of magnitude (Fig. 1E). In the absence of a carbon source or an additional hydrated electron source, CO2 reduction products were negligible, falling below detection limits of ion chromatography (IC) analysis (fig. S3). Isotopic labeling with ¹³CO₂ verified that HCOOH derived from the intended carbon source, excluding contamination. Raman spectroscopy of HCOOH produced after 3-hour irradiation with ¹³CO₂ and ¹²CO₂ revealed distinct ¹³C=O and ¹²C=O bands, with a characteristic Raman shift difference of ~24 cm⁻¹ (fig. S4). ¹³C nuclear magnetic resonance (NMR) analysis of CO₂RR products provided further evidence of ¹³C-labeled HCOOH and HCOO⁻ formation [fig. S5, aligning with a previous study (16)]. The PMEF system's efficiency also depended on anion additives generating e_{aq}^{-} , with HCOOH yields following the trend $SO_3^{2-} > I^- > Cl^-$ (fig. S6). Regardless of the e_{aq}^- source, the PMEF system consistently surpassed the bulk phase in CO₂ reduction performance. To extend the applicability of our PMEF system, we explored acetonitrile (ACN; ACN: $H_2O = 83.3\%$, v/v) and 0.1 M NaOH aqueous microdroplets. Figure S7 shows that ACN

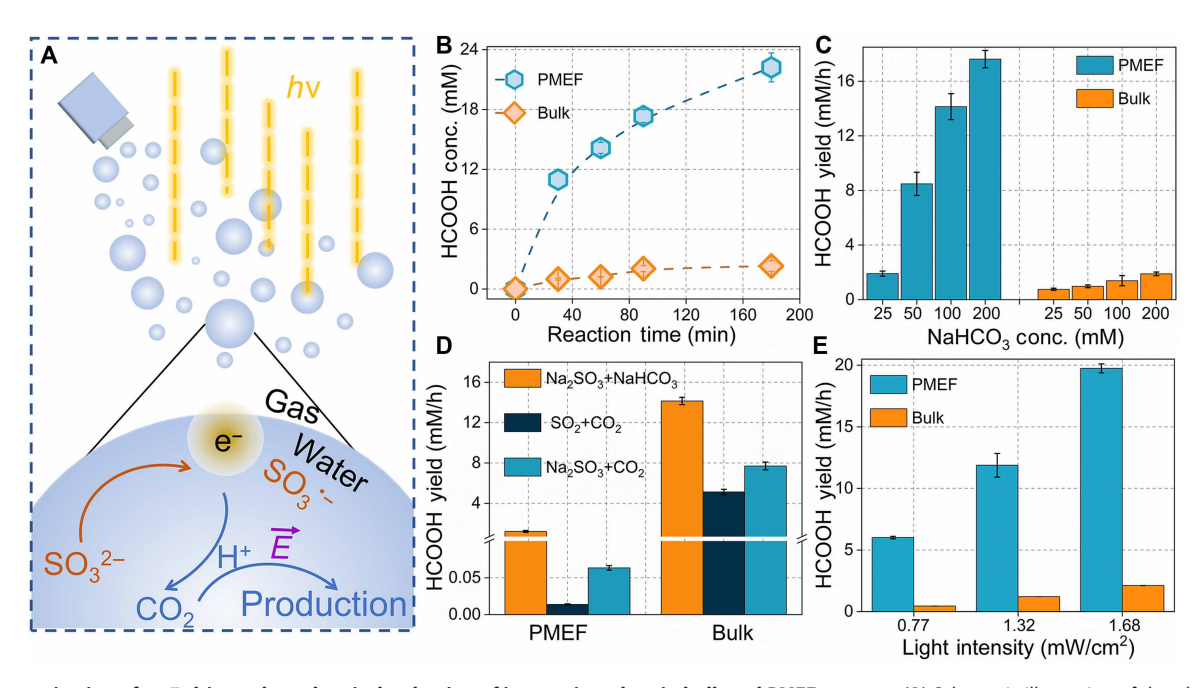


Fig. 1. Characterization of e_{aq}^- -driven photochemical reduction of inorganic carbon in bulk and PMEF systems. (A) Schematic illustration of the photochemical reaction process in the PMEF system. (B) Time-dependent HCOOH production in microdroplet (blue hexagon) and bulk (orange diamonds) reactions under light irradiation (0 to 180 min). (C) Effect of NaHCO₃ concentration on HCOOH yield in microdroplet (greenish-blue) and bulk (orange) reactions (concentrations tested: 25, 50, 100, and 200 mM). h, hour. (D) Comparison of HCOOH yield under different reaction conditions in bulk and PMEF systems. Conditions: Na₂SO₃ + NaHCO₃, Na₂SO₃ + CO₂, and SO₂ + CO₂. (E) Influence of light intensity on HCOOH yield in microdroplet (greenish-blue) and bulk (orange) reactions. Light intensities: 0.77, 1.32, and 1.68 mW/cm². Microdroplet diameter, ~300 μm. Error bars represent the standard deviation from at least three independent experiments. \vec{E} refers to the electric field, most intense at the air/water interface of microdroplet chambers.

yielded HCOOH (~158 mM/hour), surpassing NaOH (~70 mM/hour) and H_2O (~52 mM/hour), because of enhanced CO_2 solubility. These results underscore the PMEF system's exceptional photochemical CO_2RR efficiency, achieved through optimized reaction conditions and the unique properties of the microdroplet interface.

Yield and selectivity of CO₂RR products in the PMEF system under complicated condition matrices

Given the predominance of HCOOH and CH₃OH over other products, we investigated product selectivity in the PMEF system by focusing on these two species. As light intensity increased from 0.77 to 1.79 mW/cm², yields of both HCOOH and CH₃OH rose substantially (Fig. 2, A and B), driven by enhanced photon absorption that boosts electron excitation and accelerates CO₂ reduction (17). Under an argon atmosphere, HCOOH selectivity increased from 57 to 87% with rising light intensity (Fig. 2A). Introducing CO₂ further enhanced HCOOH selectivity, reaching up to 95% at the highest intensity (Fig. 2B). This improvement likely arises from the increased availability of CO₂ as a direct carbon substrate at the microdroplet interface, favoring the two-electron reduction pathway to HCOOH over competing multielectron processes like CH₃OH formation. We next explored how product selectivity varies with carbon source and concentration (Fig. 2, C and D). In an argon atmosphere, elevating NaHCO₃ concentration increased both HCOOH yield and selectivity, reflecting greater carbon availability for reduction. Unexpectedly, under a CO₂ atmosphere, both the CO₂RR rate and HCOOH selectivity declined as the NaHCO₃ concentration rose (Fig. 2D). This reversal likely stems from complex interactions among dissolved bicarbonate species (H₂CO₃/HCO₃⁻/CO₃²) and sensitive parameters (ionic strength, electric field strength, and pH) at the microdroplet interface (18). The surface accumulation of ions can intensify the interfacial electric field, altering local pH and modulating e_{aq} availability for CO₂ reduction (4, 19). In addition, reducing the microdroplet size enhanced CH₃OH selectivity and total yield under both Ar and CO₂ atmospheres (Fig. 2, E and F, and fig. S8). The observed enhancement in CH₃OH selectivity with smaller microdroplets aligns with the intensified electric field strength driven by a higher surface-to-volume ratio, as recently reported (19). Collectively, these findings highlight the PMEF system's superior photochemical CO₂RR performance, enabled by the precise control of reaction parameters and the distinct interfacial properties of microdroplets (13, 16).

Data-driven approach assisting in exploring the key parameters and forces in the PMEF system

To elucidate the influence of key variables on the PMEF system's CO_2RR performance, we introduce multiple parameters: light intensity (0.77 to 1.79 mW cm⁻²), NaHCO₃ concentration (0.05 to 0.4 mM), CO_2 concentration (0 to 1, where 0 denotes an argon atmosphere, 0.4 an air atmosphere, and 1 a high-purity CO_2 atmosphere), and microdroplet size (120 to 4572 μ m). The resulting data matrix is depicted in an alluvial diagram, illustrating the influence of these variables on product selectivity and yield (Fig. 3A and fig. S9). Small microdroplets (120 to 300 μ m) consistently yielded higher CH_3OH

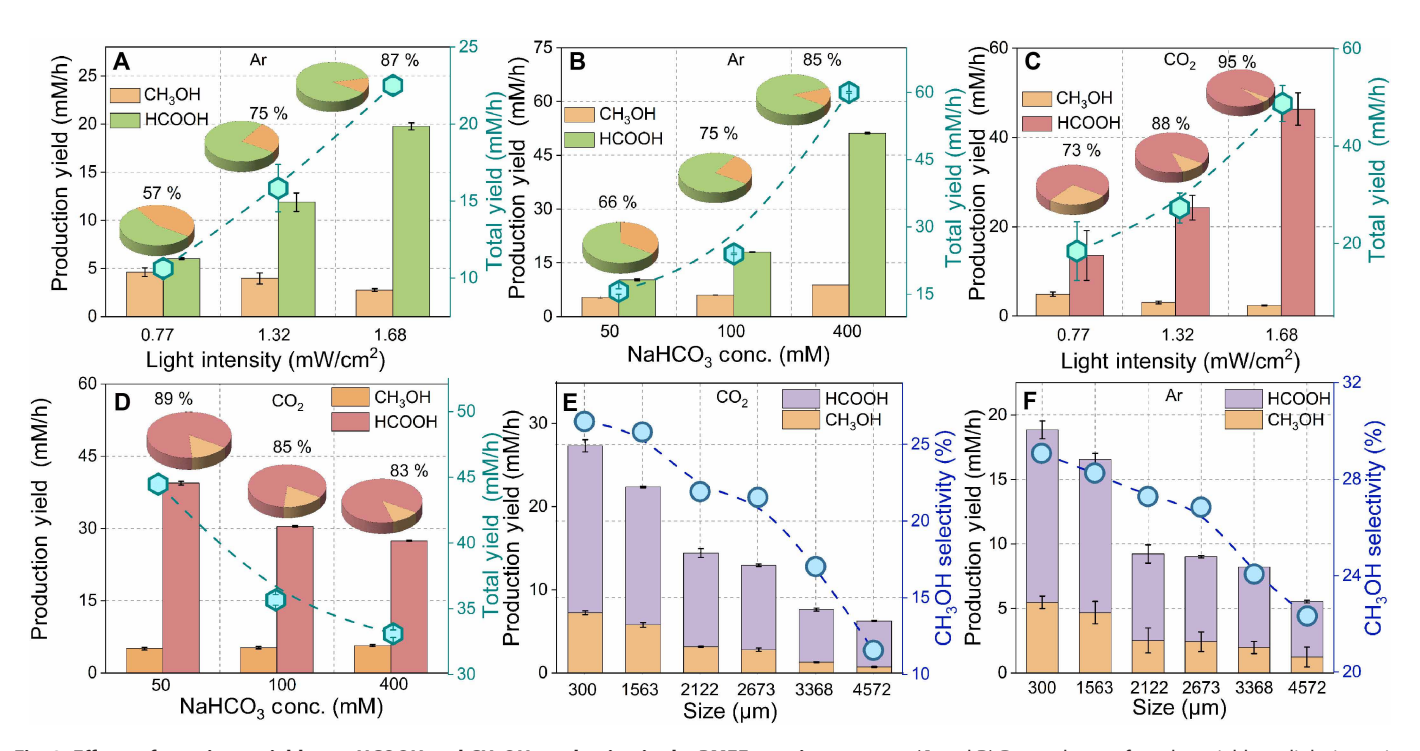


Fig. 2. Effects of reaction variables on HCOOH and CH_3OH production in the PMEF reaction systems. (A and B) Dependence of product yields on light intensity (0.77 to 1.68 mW/cm²) under Ar and CO_2 atmospheres, respectively. Pie charts illustrate product distribution, with percentages indicating HCOOH selectivity. Bar graphs display individual yields of HCOOH (light green) and CH_3OH (orange). Lavender blue plots and right y axes represent the total yield. (C and D) Effect of NaHCO₃ concentration (50 to 400 mM) under Ar and CO_2 atmospheres, respectively. Bar graphs display individual yields of HCOOH (red) and CH_3OH (orange). Lavender blue plots and right y axes represent the total yield. (E and F) Influence of microdroplet size (300 to 4572 μ m) on product yields and CH_3OH selectivity under CO_2 and Ar atmospheres, respectively. Bar graphs show yields of HCOOH (light purple) and CH_3OH (orange). The pale blue diamond symbol indicates CH_3OH selectivity (right y axis). In all panels, pie charts represent the relative abundance of HCOOH and CH_3OH .

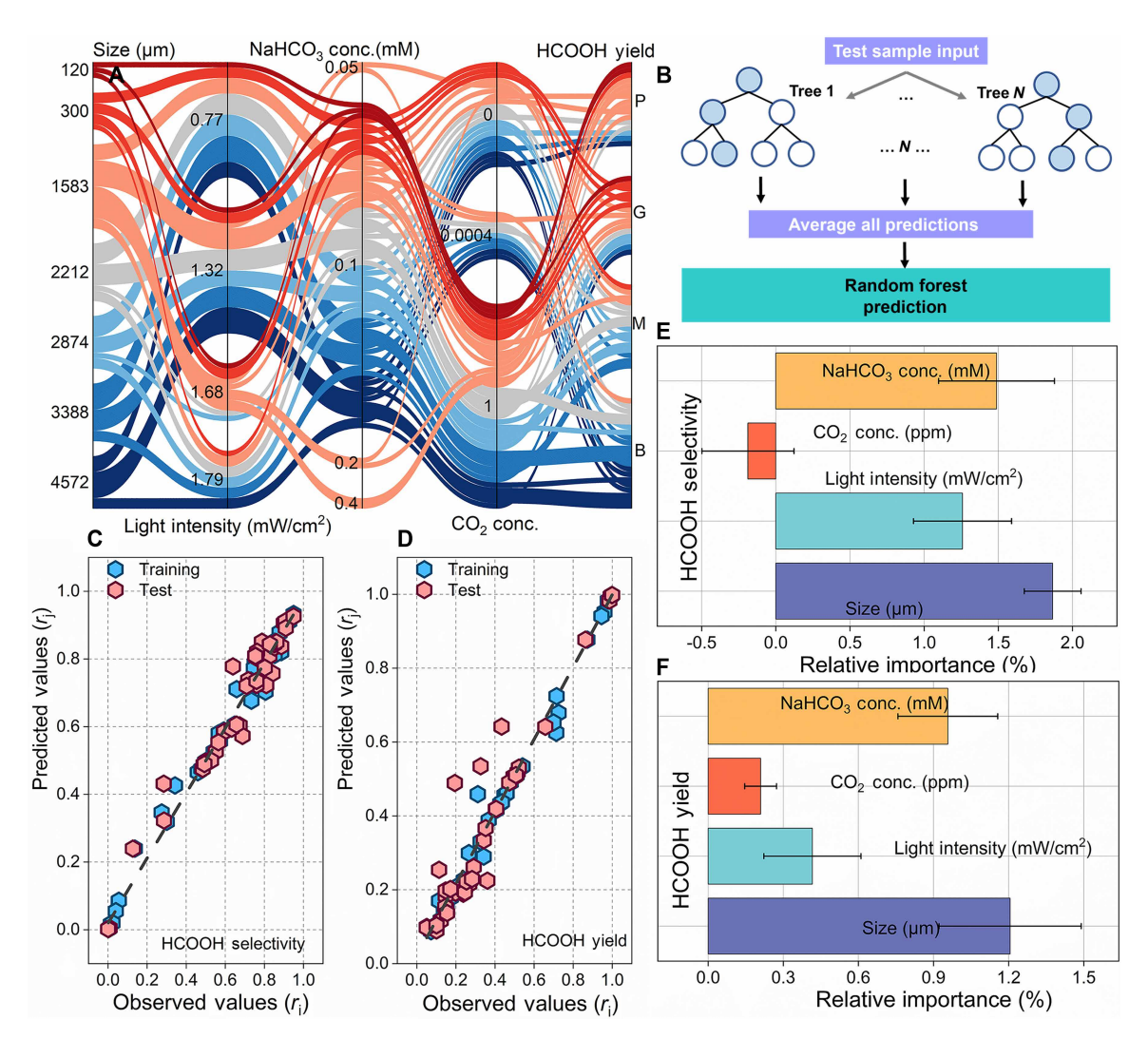


Fig. 3. Exploration of key drivers in accelerating inorganic carbon transformation in the PMEF system using the data-driven approach. (A) Parallel coordinate plot showing the impact of five key parameters—microdroplet size, NaHCO₃ concentration, HCOOH yield, light intensity, and CO₂ concentration—on the HCOOH formation process. Each line represents one experimental condition. The vertical axes indicate the experimental values for each parameter, and the flow paths between axes highlight how certain combinations of conditions are associated with higher or lower HCOOH yields. Thicker bands represent denser distributions of data points. (B) Schematic diagram of the RF model. (C and D) Comparison of observed versus predicted HCOOH yield and selectivity using the trained RF model. (E and F) Calculated relative importance of each factor contributing to HCOOH selectivity and yield. This diagram comprises five key variables: microdroplet size (120 to 4572 μm), light intensity (0.77 to 1.79 mW/cm²), NaHCO₃ concentration (0.05 to 0.4 mM), CO₂ concentration (0 represents the reaction in an argon atmosphere, 0.0004 represents the reaction in an air atmosphere, and 1 represents the reaction in a high-purity CO₂ atmosphere), and HCOOH production efficiency [categorized as perfect (P): 51.16 to 17.99 mM/hour; good (G): 17.99 to 11.87 mM/hour; moderate (M): 10.68 to 5.89 mM/hour; and bad (B): <5.89 mM/hour]. The uncertainties of the contribution of each factor to the yield and selectivity of CO₂RR products in the PMEF system were derived by running the trained RF model five times.

production and selectivity relative to HCOOH. Conversely, larger droplets and higher light intensities diminished CO₂ reduction efficiency. Increasing NaHCO₃ concentration and CO₂ availability shifted selectivity toward HCOOH. However, as the microdroplet size decreased, total yields of both HCOOH and CH₃OH rose, with CH₃OH production increasing more pronouncedly, thereby enhancing its selectivity (figs. S8 and S9). These trends underscore the critical roles of light intensity, microdroplet size, and carbon source concentration in governing CO₂RR outcomes. However, the multidimensional interplay of these factors obscures the identification of a primary driver, and conventional linear or nonlinear regression

models proved inadequate, lacking the capacity to robustly fit such complex, high-dimensional data (20).

This complexity leads us to adopt a machine learning approach, specifically a random forest (RF) model, to systematically dissect the intricate relationships governing $\rm CO_2RR$ performance in the PMEF system. Building on methodologies from our prior work (21), we constructed a decision tree–based RF model (Fig. 3B; see Materials and Methods for details) tailored to handle the high-dimensional, nonlinear interactions within our dataset. The RF model was trained on a subset of the experimental data, incorporating all four variables—light intensity, NaHCO₃ concentration, CO₂ concentration,

and microdroplet size—along with their corresponding yields and selectivities for HCOOH and CH₃OH. Hyperparameters were optimized via cross-validation to ensure robust predictive accuracy, and the model's performance was rigorously evaluated using both training and test sets. The RF model successfully reproduced HCOOH selectivity and yield with high fidelity (Fig. 3, E and F), achieving correlation coefficients exceeding 0.9 between predicted and experimental values, which underscores its reliability for further analysis. Feature importance analysis within the RF framework revealed microdroplet size as the predominant factor influencing HCOOH yield and selectivity, followed by CO₂ concentration and light intensity, with the NaHCO₃ concentration exerting a lesser but still notable effect (Fig. 3C). This size dominance likely reflects its strong correlation with the interfacial electric field strength, a key driver of reaction kinetics that activates intermediates critical to CO₂RR product formation, as detailed in the "Mechanism of the superior CO₂RR yield and selectivity in the PMEF system" section.

Photochemical inorganic carbon transformation process mediated by sulfite species

To unravel the reaction mechanism driving the high product yield and selectivity in the PMEF system, we probed the key intermediates and active species involved in the CO₂RR process. In situ Fourier transform infrared spectroscopy (FTIR; Fig. 4A) was used to monitor the photoinduced conversion of inorganic carbon in the presence of sulfite ions, while ¹H NMR spectroscopy enabled the qualitative analysis of liquid products (Fig. 4, B to F). FTIR spectra revealed distinct bands indicative of reaction intermediates. Upon accepting hydrated electrons, CO₂ is converted into a surface-bound *COOH (22) intermediate, as evidenced by the progressive growth of bands at 1782, 1771, 1753, and 1741 cm⁻¹, with subsequent steps involving *COOH potentially being rate-determining (discussion detailed in Supplementary Text S11). Subsequent electron transfer leads to the formation of HCOOH, with its C=O stretching bands appearing at 1707 (23), 1693 (24), and 1676 cm⁻¹ (25), along with C—H bending vibrations at 1425 (26) and 1408 cm⁻¹ (27). Partial dissociation of HCOOH generates HCOO⁻, which is identified by the asymmetric COO stretching bands at 1597 cm⁻¹ (28). At later stages, HCOOH and/or HCOO undergo further reduction to produce HCHO and CH₃OH. The C=O stretching mode of HCHO appears in the 1693 to 1656 cm⁻¹ (23) region, while CH₃OH formation is confirmed by the emergence of characteristic C-H and C-O vibrations at 1473 (29), 1463 (30), 1454, 1440 (31), and 1244 cm⁻¹ (23). In addition, new bands at 1560 (32),1385 (33), 1396 (34), and 1244 cm⁻¹ (23) are assigned to the S=O stretching in CH₂OH-SO₃⁻ adducts, suggesting that SO_3^{2-} plays a stabilizing role in intermediate trapping, which may influence the electron density and pathway selectivity during CO₂ conversion. The ¹H NMR spectra show characteristic chemical shifts for key CO₂ reduction products: HCOO⁻ at 8.32 parts per million (ppm) (35), CH₂(OH)SO₃⁻ at 3.52 ppm, CH₃OH at 3.20 ppm (6), and HCOH at 9.34 ppm. These signals are in good agreement with the corresponding FTIR features, collectively confirming the identity of the reduction product. On the basis of the above observations, the CO₂RR process in this system can be speculated to begin with the transfer of hydrated electrons from the sulfite surface to the surface of CO₂, leading to the activation of CO₂. The subsequent hydrogenation of the electrons leads to the production of formate, with further addition of electrons to produce CH₃OH. Besides, some trace amounts of high-value hydrocarbon by-products such as

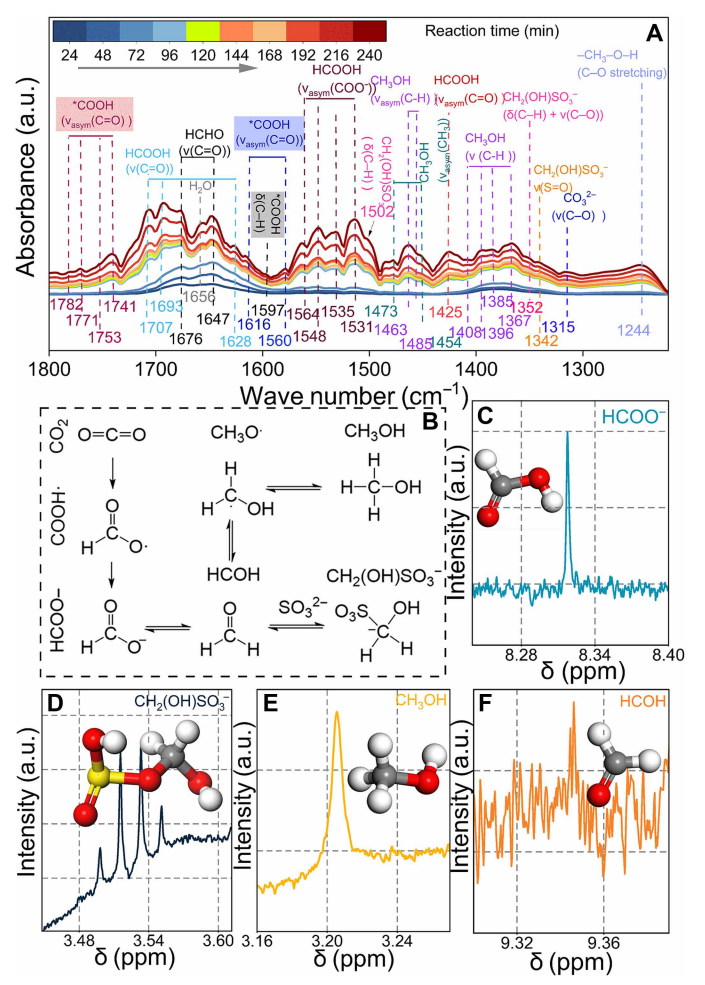


Fig. 4. Key intermediates and products in sulfite-facilitated inorganic carbon reduction. (**A**) Time-resolved in situ FTIR spectra of CO_2 photoreduction in the presence of sulfite (from 24 to 240 min). a.u., arbitrary units. (**B**) Proposed reaction pathway. ¹H NMR spectra of liquid products of (**C**) HCOOH, (**D**) $CH_2(OH)SO_3^-$, (**E**) CH_3OH , and (**F**) HCOH.

formaldehyde, oxymethyl radical, and sodium hydroxide methyl sulfate are also produced during the reaction process.

Surface propensity of sulfites and carbon sources in the PMEF system

Understanding the spatial distribution of solutes within microdroplets offers critical insights into the CO₂RR mechanism in the PMEF system. We used stimulated Raman scattering (SRS) microscopy, with its exceptional spatial resolution ($\it 19$), to map the distribution of SO₃ $^{2-}$ and HCO₃ $^{-}$ in microdroplets ranging from 22 to 160 μm (Fig. 5, A to K, and figs. S11 to S15). Both SO₃ $^{2-}$ and HCO₃ $^{-}$ ions exhibited pronounced surface propensity, with a clear size-dependent trend (Fig. 5, L to S). In larger microdroplets (diameters of 160 and 90 μm), the outermost 20% of the volume contained ~37 and 34% of the total SO₃ $^{2-}$ content, respectively. In smaller droplets (22, 36, and 60 μm), this edge region held ~31, 29, and 27%, respectively. HCO₃ $^{-}$ showed a similar but more pronounced size-dependent enrichment. We also analyzed ion distribution in larger droplets (220 to 900 μm)

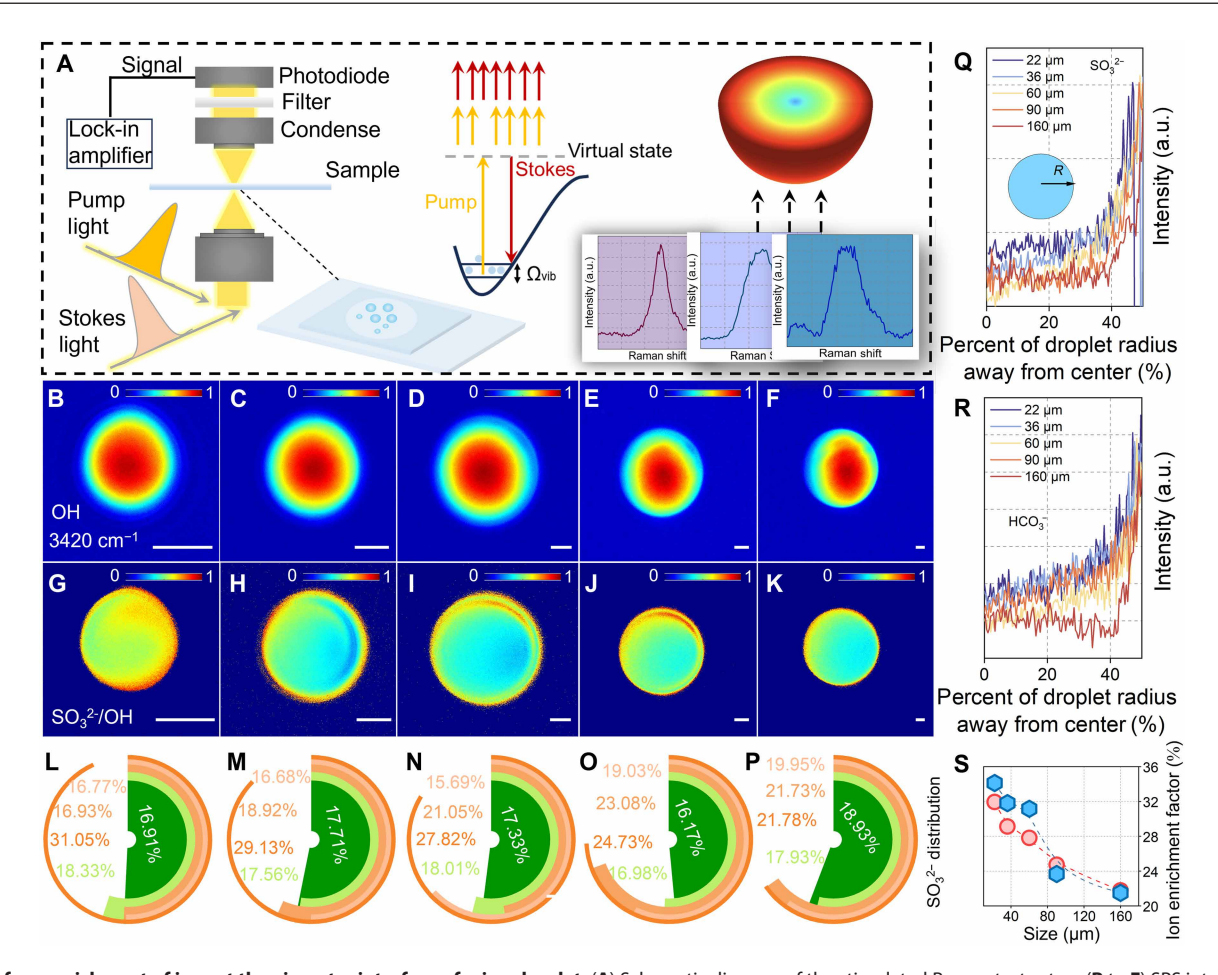


Fig. 5. Surface enrichment of ions at the air-water interface of microdroplet. (A) Schematic diagram of the stimulated Raman test setup. (B to F) SRS intensity maps of OH vibrational mode in two dimensions, illustrating the distribution of water molecules in microdroplets with diameters of 22, 36, 60, 90, and 160 μm. Scale bars, 10 μm. (G to K) Normalized concentration maps of Na_2SO_3 , obtained by using the OH signal as an internal standard. The color gradient from blue (low) to red (high) represents increasing Na_2SO_3 concentration relative to water. Microdroplets with diameters of 22, 36, 60, 90, and 160 μm. Scale bars, 10 μm. (L to P) Pie charts quantifying the distribution of Na_2SO_3 content across five concentric segments, each representing 20% of the microdroplet volume from the edge to the center. The outermost ring corresponds to the 20% volume nearest the surface. Radial distribution of (Q) Na_2SO_3 and (R) $NaHCO_3$ enrichment ratio in different size microdroplets. (5) Ion enrichment rate at the interfacial region occupying 20% of the microdroplet volume.

and found that this enrichment effect of large droplets is less evident compared to that of small droplets (fig. S16). This steep concentration gradient, likely driven by the intense interfacial electric field (19, 36), enhances local reactant availability. For HCO₃⁻, surface enrichment shifts the bicarbonate equilibrium $(HCO_3^- \rightleftharpoons CO_2 +$ OH⁻) toward CO₂ production (6), increasing its local concentration at the interface for subsequent reduction. Although higher pH generally shifts the carbonate equilibrium toward bicarbonate and carbonate species (see Supplementary Text S3 for a detailed discussion about the pH gradient effect), interfacial electric fields in microdroplets may induce localized acidification, enriching CO₂ (aq) at the droplet surface and thereby sustaining CO₂RR activity (37). Similarly, SO₃²⁻ enrichment facilitates photoinduced generation of e_{aq}, a key driver of CO₂ activation. Electron trapping experiments with CdSO₄ addition revealed a sharp drop in HCOOH yield (fig. S17), confirming e_{aq} -'s critical role. Density functional theory (DFT) results show that strong interfacial electric fields (~10⁹ V m⁻¹) confine hydrated electrons and raise the dissociation barrier, reducing the decay rate (table S2). This kinetic stabilization allows e_{aq}^{-} to persist

long enough to drive multielectron CO₂ reduction (fig. S19 and Supplementary Text S12).

Surface enrichment of SO₃²⁻ ions at the air/water interface of the microdroplet allows us to speculate a high concentration level of hydrated electrons over the microdroplet surface, as well evidenced by the observation of a prolonged lifetime of hydrated electrons at the interface using nanosecond transient absorption spectroscopy (NTAS; schematic chart available in fig. S18). To quantify the interfacial electric field driving this effect, we used Au nanoparticles functionalized with sodium thiocyanate (NaSCN) as probe molecules, measuring the Raman Stark shift ($\Delta\omega_{C-N}$) across microdroplet interfaces and interiors (fig. S20). Consistent with the established Stark effect relationship ($E = \Delta \omega_{C-N}/0.36 \text{ MV cm}^{-1}$) (38, 39), where the electric field strength scales with spectral shift, we observed a pronounced size-dependent increase. As the microdroplet diameter decreased from 150 to 26 µm, the Stark shift rose from 9 to 27 cm⁻¹, corresponding to an electric field intensification from 25 to 75 MV cm⁻¹. This field enhancement, orders of magnitude stronger than in bulk, extends $e_{aq}^{}$ lifetime by several orders of magnitude at the gas-liquid interface (Fig. 6, A to C), directly facilitating CO₂ reduction. These findings highlight the interfacial electric field's pivotal role in stabilizing reactive species and boosting CO₂RR efficiency in the PMEF system. Overall, the primary active site is provided by the surface region where hydrated electrons interact with CO₂ molecules at the gas-liquid interface of microdroplets. This is well supported by recent milestone studies adopting the scaling law for exploring the aqueous reactions in microdroplets (40, 41).

Mechanism of the superior CO₂RR yield and selectivity in the PMEF system

Strong electric fields at microdroplet air-water interfaces are known to enhance ion enrichment, lower reaction energy barriers, and accelerate kinetics by stabilizing transition states or amplifying molecular dipoles (42). To probe this effect in the PMEF system, we applied an electric field strength matching our measured values (25 to 75 MV cm⁻¹; Fig. 6D and fig. S19) to evaluate free energy changes in key CO₂RR intermediates and products during photoreduction with sulfite. On the basis of the above results and literature reports, we can infer that the CO_2 activation process is mediated by e_{aq} . Specifically, the CO₂ molecule begins with a linear structure of zero dipole moment, along with each oxygen atom harboring a lone pair of electrons that can donate to Lewis acid centers. The subsequent reaction between the H₃O radical and CO₂ is a proton-coupled electron-transfer process, where an electron is transferred from the hydrated H₃O radical (donor) to the CO2 molecule (acceptor). The electron transfer is coupled with proton transfer from the donor to the acceptor and leads to the bending of the CO₂ molecule. Upon the addition of electrons to CO_2 , the π^* antibonding orbital is filled, which increased free energy and electron cloud contraction because of carbon atom rehybridization. For this free anion radical, the electric field results in the unpaired electrons in the antibonding orbitals, making the C—O bond longer and unstable. In the important proton-coupled electron-transfer process, the free energies in the electric field case are decreased by 2.9 kJ/mol compared to those in the non–electric field case. The decrease in free energy in the CO_2 activation step explains the increase in CO_2 reduction efficiency in microdroplets of the strong electric field relative to the bulk phase free of this field.

From the orbital perspective, a strong electric field at the microdroplet lowers the lowest unoccupied molecular orbital (LUMO) of CO₂, contributing to the strengthened electron acquisition ability of CO₂. Besides, the strong electric field decreases the bond angle and increases the bond length of key intermediates and active species, thus leaving a less stable chemical structure for subsequent reactions. In addition, the C=O bond is less stable relative to that of CO₂• in the electric field–free case, with the bond angle of O=C=O prolonged from 143.78° to 143.98°. The ΔG values of HCOH reduction to CH₃OH and hydroxymethane sulfonate [CH₂(OH)SO₃⁻] in a bulk solution free of the electric field are 71.4 and 114.82 kJ/mol, while they are 65.62 and 111.92 kJ/mol in the presence of a strong electric field available over the air/water interface of microdroplets, respectively. This reduction in ΔG , driven by field-induced destabilization, accelerates the multielectron pathways, contributing to the enhanced yield and selectivity of CH₃OH in the PMEF system.

The energy barrier for CH₃OH formation exceeds that of HCOOH, consistent with HCOOH's preferential production in the PMEF system

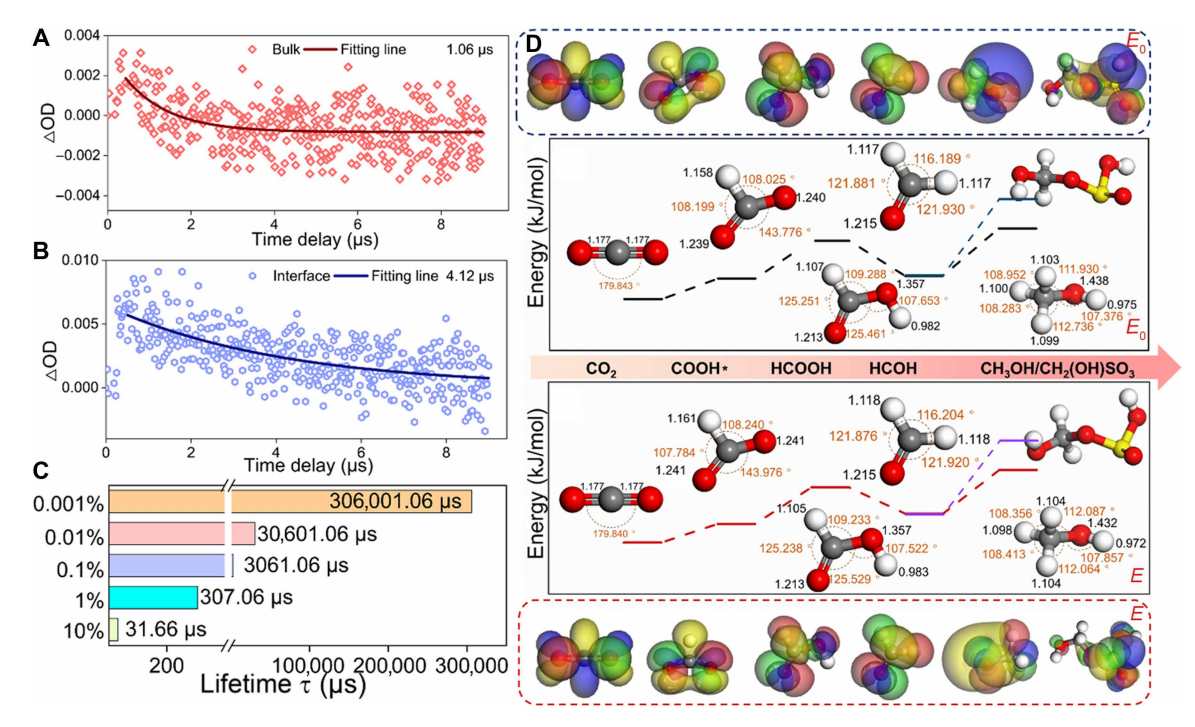


Fig. 6. Lifetime analysis of electron and free energy profiles of the key CO_2 reduction pathway in bulk (free of electric field) and air/water interface of the strong electric field. (A and B) NTAS analysis of the lifetime of e_{aq}^- at the interface and bulk (inset graph: NTAS test window of the absolute bulk and gas-liquid interface—containing solution). Δ OD, change in optical density. (C) Calculation of the overall interfacial decay rate of e_{aq}^- by assuming different abundances of air/water interfaces (more details available in Materials and Methods). (D) Energy diagram showing the reaction pathway for CO_2 reduction. Frontier orbital visualizations (HOMO and LUMO) for key species in the reduction pathway. The HOMO [purple (+) ...green (–) wave function] and LUMO [pink (+) ... blue (–) wave function] are shown with the wave function isosurfaces plotted at the same isovalue.

because of its lower electron demand (two versus six electrons). The highest occupied molecular orbital (HOMO) energy, linked to ionization potential via Koopmans' theorem, and the LUMO energy, indicative of electron affinity, govern CO2's reactivity. In its neutral state, CO₂'s central carbon exhibits a spherically symmetric electron cloud, diminishing radially outward (43). Under the microdroplet's strong electric field, the LUMO of CO₂ decreases by 0.34 kJ mol⁻¹ (table S3), enhancing its electron-accepting capacity and facilitating e_{aq} -driven activation. For HCHO, a key intermediate product route to CH₃OH, the LUMO drops by 0.53 kJ mol⁻¹ in the field, further promoting redox steps. This orbital stabilization correlates with increased CH₃OH yield as the microdroplet size decreases, amplifying the interfacial electric field (fig. S21). Smaller droplets thus lower the effective energy barrier for CH₃OH formation by destabilizing intermediate products like HCHO, evidenced by elongated C-O and H—O bonds. The PMEF system's CO₂ reduction primarily occurs at the air-water interface, enhanced by the synergistic effects of interfacial electric fields, hydrated electrons, SO_3^{2-} photodetachment, pH-driven proton sources, and accelerated SO_3^{2-} photolysis, driving multielectron pathways to HCOOH and CH3OH (discussion detailed in Supplementary Texts S5 to S10, S13, and S14). Collectively, these field-induced effects—orbital energy reduction and bond instability—underpin the PMEF system's enhanced photochemical CO₂RR performance, reducing barriers for inorganic carbon reduction and steering selectivity toward high-value products.

Scale-up attempts and potential application of the PMEF system

Building on our understanding of key drivers—most notably the intensified interfacial electric field in smaller microdroplets—we scaled up the PMEF system to validate its CO₂RR efficiency for practical CO₂ utilization. Using a commercial nebulizer, we sprayed an aqueous precursor solution into a reactor, generating continuous microdroplets (<10-μm diameter; Fig. 7, A and B). For comparison, a stirred bulk solution of equal volume served as a control. After 10 hours, the PMEF system yielded 1009.25 mmol of HCOOH and CH₃OH combined (quantified by a turnover number of 10³ to 10⁴; discussion detailed in Supplementary Text S6), a 144- to 628-fold increase over the bulk control (Fig. 7, C to F), aligning with predictions of enhanced yield and CH₃OH selectivity from downsizing microdroplets. These yields surpass traditional catalytic systems by two to four orders of magnitude and, in some cases, up to seven orders (Fig. 7E and table S4). Our laboratory results further corroborate that CH₃OH selectivity increases with decreasing droplet size, reaching ~99% in the scaled system because of the intense interfacial electric field (Fig. 7D).

However, the current setup revealed limitations. The nebulizer sprayed only a fraction of the solution, leaving most as bulk media below the nozzle. Assuming that 1 to 10% of the volume persists as microdroplets, we estimate potential yield increases of two or three orders for HCOOH and three or four orders for CH₃OH with a fully optimized setup. Additional challenges include light attenuation from dense microdroplet clouds, reducing downward irradiance, and short droplet residence times, as many adhere to reactor walls before returning to the bulk (Fig. 7A). These factors constrain efficiency in the present configuration. Future efforts will focus on refining the PMEF reactor (Fig. 7G) to maximize microdroplet generation, light penetration, and residence time, aiming for broader industrial applicability in sustainable CO₂ conversion (discussion detailed in Supplementary Text S15).

DISCUSSION

This study introduces a plausible approach for CO₂ reduction through the utilization of hydrated electrons generated within microdroplets under intense electric fields, delivering unprecedented efficiency and selectivity. By integrating machine learning with advanced experimental techniques, we established that microdroplet size and interfacial electric fields profoundly enhance CO₂ reduction—producing HCOOH and CH₃OH at rates up to seven orders of magnitude higher than conventional systems. The strong interfacial electric fields (10⁹ V m⁻¹) extend the lifetime of hydrated electrons by orders of magnitude, facilitate ion accumulation at interfaces, and destabilize chemical bonds in key intermediates, thereby lowering energy barriers for inorganic carbon reduction and directing reaction selectivity. Notably, we demonstrated that industrial waste-derived sulfite ions can produce superior hydrated electrons (eaq) to efficiently convert CO2 into targeted hydrocarbon fuels with nearly 100% selectivity, representing a substantial advancement in photochemical CO₂ conversion. Beyond atmospheric carbon management, these insights open possibilities in green chemistry, industrial catalysis, and materials synthesis, establishing a scalable framework for sustainable carbon-neutral fuel production that addresses both energy demands and climate challenges simultaneously. We note, however, that contaminants such as NO_x and soot may disrupt the redox environment, warranting further investigation under real flue gas conditions. Future applications may involve a modular cascade system integrating upstream scrubbing and droplet-based conversion, offering a scalable and energy-efficient route for CO₂ utilization.

MATERIALS AND METHODS

Photochemistry CO₂RR

All reagents were purchased from Aladdin and used without additional purification (Supplementary Text S1). Unless specified otherwise, 500 mM Na₂SO₃ and 100 mM NaHCO₃ were used as the precursor solution. All experiments were repeated at least three times, with the typical experimental procedures schematically illustrated in fig. S1. Following the protocol outlined in our previous work (36), microdroplets were initially generated using an atomizer on the prepared superhydrophobic quartz wafer. Afterward, these microdroplets were introduced into a custom-designed reactor, where humified CO_2 or Ar flow (RH = ~90%) was purged, with the deposited microdroplets of various sizes balanced for 10 min before starting the light experiments. This step essentially enables the size stabilization of microdroplets throughout the reaction, as confirmed by the optical images captured by the Raman microscope (2). For bulk phase photochemical CO₂RR experiments, 3 ml of aqueous solution was added to a quartz petri dish (diameter, 30 mm) and performed in a custom-designed quartz reactor (RH = ~90%; fig. S1). The microdroplets were collected at a specified time and diluted using a known volume of deionized water for further analysis. The liquidphase products were filtered through a polytetrafluoroethylene membrane filter (diameter, 220 nm) and then analyzed using a Metrohm 883 Basic IC system equipped with a Metrosep A supply 5-250/4.0 analytical column and a conductivity detector. HCOOH and HCOO concentrations were quantified using IC, with a NaHCO₃ + Na₂CO₃ solution used as the eluent. By applying this elution (used in excess relative to the sample), any HCOOH present in the sample is fully deprotonated to HCOO-, ensuring that the total formate signal corresponds to the sum of both species. This analytical setup allows

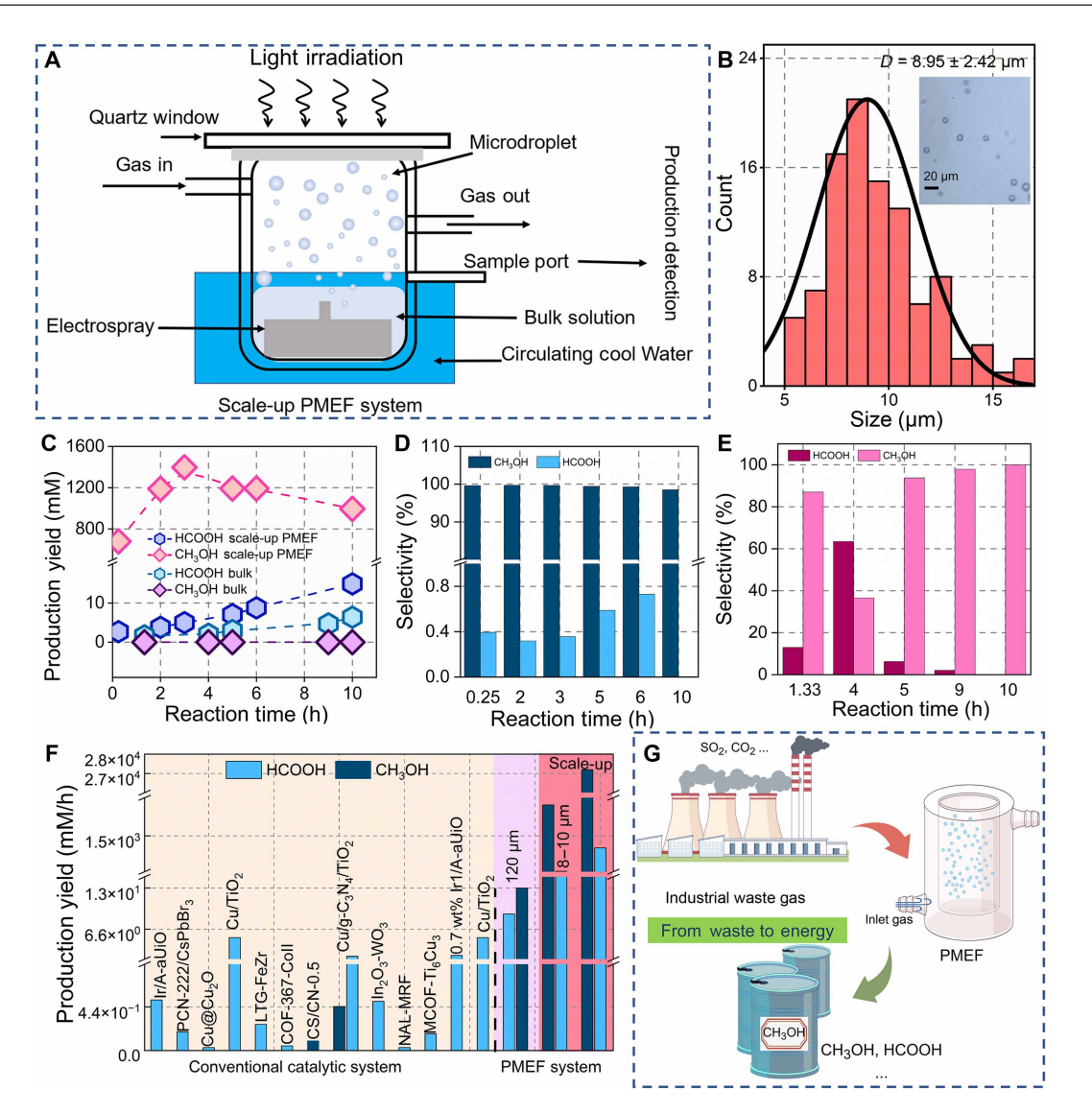


Fig. 7. Scale-up PMEF system for CO₂ reduction product yield and selectivity. (A) Schematic diagram illustrating the large-scale CO₂ reduction process. (B) Size of the microdroplet produced by electrospray. (C) Yield of production (mmol) over time (hour) for different conditions, including CH₃OH and HCOOH from both electrospray microdroplet and bulk solution in a large-scale setup. (D and E) Selectivity percentages for CH₃OH and HCOOH at various time points during the large-scale experiment in bulk solution and microdroplet reaction. (F) Comparisons between the yield of HCOOH and CH₃OH produced in the PMEF system (this work) and the previous observation in bulk solution (more relevant data detailed in table S4). (G) Schematic concept of conversion of industrial waste CO₂ and SO₂ to hydrocarbon fuels by using the proposed PMEF system.

for precise quantification of total formate content. The effect of environmental factors on HCOOH yield discussion is detailed in Supplementary Text S2. The gas-phase products were detected using a gas chromatography-thermal conductivity detector/flame ionization detector (GC-TCD/FID) instrument (equipped with a methane reformer and a 5-Å molecular sieve packing column, Shimadzu GC-2014) with a 5-Å molecular sieve packing column. CH₃OH was detected by a GC-TCD/FID, which is equipped with a highly efficient capillary analysis column (ON-FFAP, 30 by 0.32 by 0.25). The gas flow rates were 30 ml min $^{-1}$ (H₂), 300 ml min $^{-1}$ (air), and 30 ml min $^{-1}$ (N₂). The injector, TCD, and FID temperatures were 150°, 200°, and 150°C, respectively. 1 H NMR spectroscopy and 13 C NMR spectroscopy were conducted using a Bruker Ascend 400-MHz spectrometer.

Principle and control measures for maintaining microdroplet stability

The dissolved salts increase the internal osmotic pressure ($\pi = iMRT$), creating a thermodynamic driving force that opposes water loss and even promotes deliquescence under high-RH conditions (44). This osmotic stabilization slows down shrinkage and helps the droplet maintain its volume over long durations. On the other hand, high salt concentrations (0.5 M Na₂SO₃ and 0.05 to 0.4 M NaHCO₃) substantially reduce the water activity (a_x) within the droplets by forming extensive ion hydration shells. This reduces the vapor pressure of the droplet (per Raoult's Law), thereby suppressing evaporation (45).

Besides, to ensure the stability of microdroplets during the reaction process, we implemented a rigorous control method tailored to the experimental setup. After generating droplets of specific sizes

using a nebulizer on a superhydrophobic substrate, the hydrophobic quartz slide was placed in a sealed reaction chamber. High-humidity gas was introduced to maintain an RH of ~90%, effectively minimizing rapid evaporation, as confirmed by the bright-field image showing marginal size changes under light illumination throughout the reaction process (fig. S2). The size of droplets shows a negligible change in the chamber, with product yields and selectivity averaged from multiple runs to mitigate measurement bias or uncertainties.

Machine learning

In this research, we implemented a decision tree as an inductive learning method using collected laboratory datasets for machine learning. This numerical technique produces a tree-like framework to define classification rules, with more explanation of the construction of decision trees detailed in an earlier study (21). Given the obtained lab-based results, we eventually produced data matrices of 90 by 6 using the initial 45 sets as a training group to develop the decision tree model, while the other 45 sets were used as a test group to evaluate the performance of the model predictions. The discussion about machine learning validation and interpretation is detailed in Supplementary Text S4. The RF classifier was formed by randomly sampling from the training data, creating independent decision trees, and combining their results for the final prediction. All predictions and computations were performed using the Random Forest Toolbox in MATLAB 2021b (MathWorks). After constructing the decision tree, we assessed the performance of the trained model by calculating various metrics on the test dataset, including the coefficient of determination (R^2) , root mean square error (RMSE), mean bias error (MBE), and mean absolute error (MAE) using the following equations

$$R^{2} = \frac{\left[\sum_{i=1}^{m} (X_{i} - \overline{X}) (Y_{i} - \overline{Y})\right]}{\sum_{i=1}^{m} (X_{i} - \overline{X})^{2} (Y_{i} - \overline{Y})^{2}}$$
(1)

$$RMSE = \sqrt{\frac{\sum_{i=1}^{m} (Y_i - X_i)^2}{m}}$$
 (2)

$$ME = \frac{\sum_{i=1}^{n} (Y_i - X_i)}{n}$$
(3)

$$MAE = \frac{\sum_{i=1}^{m} |Y_i - X_i|}{m}$$
(4)

where X_i and Y_i denote the measured values and predicted values, respectively. In this study, the use of a set of 500 uncorrelated decision trees resulted in strong predictive performance for the HCOOH removal efficiency index, achieving training $R^2 = 0.95319$ and test $R^2 = 0.91234$. The results and discussion of the *K*-fold cross-validation are provided in fig. S10 and Supplementary Text S4.

Raman measurement

For characterizing the strength of the electric field within the microdroplets, the Raman measurements were performed with an XploRA Plus confocal Raman spectrometer (Jobin Yvon, HORIBA, Gr, France) coupled with a 10× Olympus microscope objective (Olympus, 0.9 numerical aperture). An external-cavity diode laser (532 and 785 nm) was used for excitation. The Raman signal was collected using a multichannel electron-multiplying charge-coupled device ranging from 400 to 4200 cm⁻¹, with two spectrum accumulations at a 10-s acquisition time per spectrum. The Raman data analyses including baseline removal by a polynomial equation and spectral fitting with the Gauss-Lorenz function were conducted using LabSpec 6 software.

Measurement of the interfacial electric field of microdroplets

NaSCN was selected as a vibrational Stark probe owing to the pronounced electric field sensitivity of its $C\equiv N$ stretching mode. To construct a surface-enhanced Raman scattering-active interface, 500 μ l of citrate-stabilized gold nanoparticles (\sim 50-nm diameter) was mixed with 250 μ l of 4 M NaSCN, enabling SCN $^-$ ions to self-assemble on the Au surface. The resulting colloid was aerosolized into microdroplets over the hydrophobic substrate and sent into a flow-cell reactor maintained at \sim 90% RH. Raman spectra were recorded within 30 min to minimize potential deactivation of probes.

To determine the electric field strength at the gas-liquid interface of the microdroplet, the Raman shift difference of $\nu(C\equiv N)$ at the interface and at the center ($\Delta\nu_{CN}=\nu_{CN_interface}-\nu_{CN_center}$) was used to calculate the following equation (46), considering that the net center bulk region is free of electric field (36, 47)

$$EF = \Delta\omega_{CN} \times \Delta\nu_{CN} \tag{5}$$

where $\Delta\omega_{CN}$ is an established vibrational Stark tuning rate (0.36 MV cm⁻¹), and $\Delta\nu_{CN}$ refers to the determined Stark frequency shift (cm⁻¹) determined by the surface-enhanced Raman scattering analysis.

The custom-built SRS microscope, based on a dual-output femtosecond laser system (Insight DS+, Spectra-Physics), enabled highresolution chemical imaging of SO₃²⁻, HCO₃⁻, and H₂O. The 1040-nm fixed output served as the Stokes beam, while the tunable output (680 to 1300 nm) acted as the pump beam. Spectral resolution was enhanced to ~13 cm⁻¹ by stretching both pulses to picosecond durations using SF57 glass elements. An electro-optical modulator modulated the Stokes beam at 20 MHz. For mapping analysis, the pump laser was tuned to 941 nm for SO_3^{2-} and HCO_3^{-} and 776 nm for H₂O. Using a water-immersion objective (numerical aperture, 1.2) and appropriate pixel sampling, we achieved an effective spatial resolution of ~340 nm. This SRS setup, leveraging the quadratic dependence of the signal on excitation intensities, provided label-free, high-sensitivity imaging of target molecules at the focal spot, making it an ideal technique for acquiring the spatially high distribution of solutes within the microdroplets.

¹³C isotopic experiment

Either ¹³CO₂ or ¹²CO₂ was bubbled into a Na₂SO₃ solution for 30 min, followed by the resulting ¹³CO₂-saturated and ¹²CO₂-saturated solutions as the stock solution to produce microdroplets for the subsequent CO₂RR in the reactor (fig. S1). The resulting H¹²COOH and H¹³COOH products in microdroplets after a reaction of 180 min under light irradiation were detected by a confocal Raman spectrometer, with test parameters and settings detailed elsewhere (36).

Transient absorption spectrum measurements

The lifetime of e_{aq} at the gas-liquid interface regions and in bulk solution was measured using NTAS (NTAS-100, Dalian Institute of Chemical Physics, China). A detailed schematic and protocol for the laser flash photolysis-long-path absorption apparatus can be found in our previous work (42). Briefly, a Nd:yttrium-aluminum-garnet laser source (266 nm, pulse duration of 9 ns) with an energy of ~5 mJ was used as the pump light and introduced into the Suprasil self-masking cuvettes (1-cm optical path length and an actual volume of 4 ml). All transient absorption spectra were recorded at 298 K, with the results obtained from averaging the spectra over 20 measurements. The entrance slit of the monochromator was consistently set to 1 mm for all experiments.

To investigate the interfacial decay kinetics using NTAS measurements, we adjusted the height of Na₂SO₃ (0.5 mM) solution in the sample holder, creating two scenarios: "absolute bulk" and "airwater interface–containing" (as illustrated in the inset of fig. S17, where the circular window indicates the laser beam path). In the "absolute bulk" setup, the laser beam directly irradiates the Na₂SO₃ solution without any interfaces, while in the "air-water interface–containing" scenario, the laser beam interacts with the Na₂SO₃ solution that includes both interfaces and bulk solution. For both scenarios, we determined the lifespan of $e_{\rm aq}^-$ generated at the interface and in the bulk solution by monitoring the corresponding decay dynamics. A single-exponential decay curve (Eq. 6) was used to fit the observed results

$$y = a + be^{-\frac{x}{\tau}} \tag{6}$$

where τ refers to the obtained half-lifetime of e_{aq}^- . This equation allows us to obtain the half-lifetime T_b and T_i of e_{aq}^- in both "absolute bulk" and "gas-liquid interface–containing" scenarios. We assumed that T_i is a rate lifetime correlated to T_m (referring to the lifetime of e_{aq}^- at the interface) and T_b (referring to the lifetime of e_{aq}^- in the bulk) and their corresponding abundance (T_i and T_b) in the sample, and we then established an equation (Eq. 7) through a simple linear superposition

$$T_{\rm m} = T_{\rm i} \times \tau_{\rm i} + \left(1 - T_{\rm i}\right) \times \tau_{\rm b} \tag{7}$$

 $T_{\rm i}$ denotes the abundance of the air-water interface, while $(1-T_{\rm i})$ represents the bulk phase abundance. The half-lifespans of $e_{\rm aq}^-$ at the interface were determined to be 31.66 μs^{-1} (assuming that the volume of the interface constitutes 10% of the bulk solution) and $3.06 \times 10^5 \,\mu s$ (assuming that the interface volume constitutes 0.001% of the bulk solution), which are one and five orders of magnitude greater than that in the bulk phase (Fig. 6C).

Computational details

First-principles calculations were carried out on the basis of periodic DFT using a generalized gradient approximation within the Perdew-Burke-Ernzerhof exchange correction functional. The wave functions were constructed from the expansion of plane waves with an energy cutoff of 450 eV. Gamma-centered k-points of 2 by 2 by 2 have been used for geometry optimization. The consistency tolerances for the geometry optimization are set as 1.0×10^{-6} eV atom⁻¹ for the total energy and 0.02 eV/Å for the force. In free energy calculations, the entropic corrections and zero-point energy (ZPE) have been included. The free energy of species was calculated according to the standard formula

$$\Delta G = E + \Delta ZPE + \Delta H - \Delta TS \tag{8}$$

where ZPE is the zero-point energy, ΔH is the integrated heat capacity, T is the temperature of the product, and S is the entropy. The frontier molecular orbitals, HOMO and LUMO, along with the Mulliken charges of all chemical structures in the DFT calculations, were further visualized using the DMol3 package integrated into the Materials Studio software suite. Quantum chemical features of interest, such as the average orbital energies of the HOMO (EHOMO) and LUMO (ELUMO) and the corresponding energy gap (DE = EHOMO – ELUMO), were accordingly obtained. The black dashed lines indicate the measured bond lengths of the molecules or intermediates at each reaction step, while the pink dashed lines represent the close contacts between atoms in the molecules.

Supplementary Materials

This PDF file includes:

Supplementary Text S1 to S15 Figs. S1 to S21 Tables S1 to S4 References

REFERENCE AND NOTES

- Q. Zhu, Z. Deng, H. Xie, M. Xing, J. Zhang, Investigation of concerted proton–electron donors for promoting the selective production of HCOOH in CO₂ photoreduction. ACS Catal. 13. 3254–3262 (2023).
- 2. A. J. Swallow, Hydrated electrons in seawater. Nature 222, 369-370 (1969).
- G. Liu, C. Feng, P. Shao, Degradation of perfluorooctanoic acid with hydrated electron by a heterogeneous catalytic system. Environ. Sci. Technol. 56, 6223–6231 (2022).
- C. K. Amador, H. Cavalli, R. Tenorio, H. Tetu, C. P. Higgins, S. Vyas, T. J. Strathmann, Influence of carbonate speciation on hydrated electron treatment processes. *Environ. Sci. Technol.* 57, 7849–7857 (2023).
- E. J. Hart, S. Gordon, E. M. Fielden, Reaction of the hydrated electron with water. J. Phys. Chem. 70, 150–156 (1966).
- Z. Liu, L.-F. Wu, C. L. Kufner, D. D. Sasselov, W. W. Fischer, J. D. Sutherland, Prebiotic photoredox synthesis from carbon dioxide and sulfite. *Nat. Chem.* 13, 1126–1132 (2021).
- Y. Liu, Q. Ge, T. Wang, R. Zhang, K. Li, K. Gong, L. Xie, W. Wang, L. Wang, W. You, X. Ruan, Z. Shi, J. Han, R. Wang, H. Fu, J. Chen, C. K. Chan, L. Zhang, Strong electric field force at the air/ water interface drives fast sulfate production in the atmosphere. *Chem* 10, 330–351 (2024).
- B. S. Mu, Y. Zhang, M. Peng, Z. Tu, Z. Guo, S. Shen, Y. Xu, W. Liang, X. Wang, M. Wang, D. Ma, Z. Liu, Radiocatalytic synthesis of acetic acid from CH₄ and CO₂. Angew. Chem. Int. Ed. Engl. 136, e202407443 (2024).
- A. Lisovskaya, D. M. Bartels, Reduction of CO₂ by hydrated electrons in high temperature water. Radiat. Phys. Chem. 158, 61–63 (2019).
- X. Li, J. Yu, M. Jaroniec, X. Chen, Cocatalysts for selective photoreduction of CO₂ into solar fuels. Chem. Rev. 119, 3962–4179 (2019).
- Y. Meng, Y. Xia, J. Xu, R. N. Zare, Spraying of water microdroplets forms luminescence and causes chemical reactions in surrounding gas. Sci. Adv. 11, eadt8979 (2025).
- 12. M. F. Ruiz-Lopez, J. S. Francisco, M. T. C. Martins-Costa, J. M. Anglada, Molecular reactions at aqueous interfaces. *Nat. Rev. Chem.* **4**, 459–475 (2020).
- K. R. Wilson, A. M. Prophet, Chemical kinetics in microdroplets. Annu. Rev. Phys. Chem. 75, 185–208 (2024).
- S. Wang, S. Shan, S. Xiao, F. Liu, Z. Yang, S. Li, Z. Qiu, X. Dong, Y. Cheng, X. Zhang, Spontaneously generated electrons for CO₂ hydrogenation to formate at the microinterface of air-water. Adv. Energy Mater. 13, 2303121 (2023).
- C. J. C. Jordan, M. P. Coons, J. M. Herbert, J. R. R. Verlet, Spectroscopy and dynamics of the hydrated electron at the water/air interface. Nat. Commun. 15, 182 (2024).
- S. Chen, L.-H. Chung, S. Chen, Z. Jiang, N. Li, J. Hu, W.-M. Liao, J. He, Efficient lead removal by assembly of bio-derived ellagate framework, which enables electrocatalytic reduction of CO₂ to formate. Small 20, e2400978 (2024).
- X. Shi, W. Peng, Y. Huang, C. Gao, Y. Fu, Z. Wang, L. Yang, Z. Zhu, J. Cao, F. Rao, G. Zhu, S. Lee, Y. Xiong, Integrable utilization of intermittent sunlight and residual heat for on-demand CO₂ conversion with water. *Nat. Commun.* 15, 10135 (2024).
- S. Fang, M. Rahaman, J. Bharti, E. Reisner, M. Robert, G. A. Ozin, Y. H. Hu, Photocatalytic CO₂ reduction. *Nat. Rev. Methods Primers* 3, 62 (2023).
- K. Gong, J. Ao, K. Li, L. Liu, Y. Liu, G. Xu, T. Wang, H. Cheng, Z. Wang, X. Zhang, H. Wei, C. George, A. Mellouki, H. Herrmann, L. Wang, J. Chen, M. Ji, L. Zhang, J. S. Francisco,

SCIENCE ADVANCES | RESEARCH ARTICLE

- Imaging of pH distribution inside individual microdroplet by stimulated Raman microscopy, *Proc. Natl. Acad. Sci. U.S.A.* **120**, e2219588120 (2023).
- Y. Liu, T. Wang, Q. Ge, W. You, K. Li, W. Wang, L. Xie, L. Wang, X. Fang, X. Ruan, L. Yang, R. Wang, L. Zhang, Unveiling the role of carbonate radical anions in dust-driven SO₂ oxidation. J. Geophys. Res. Atmos. 129, e2023 JD040017 (2024).
- Y. Liu, Q. Ge, T. Wang, K. Li, Y. Deng, W. You, L. Xie, L. Zhang, Investigating the impact of pretreatment strategies on photocatalyst for accurate CO₂RR productivity quantification: A machine learning approach. *Chem. Eng. J.* 473, 145255 (2023).
- S. Deng, R. Cao, X. Wang, Y. Zhou, J. Liang, H. Tang, X. Feng, S. Yang, Y. Shangguan, Y. Li, H. Chen, Upconversion phosphor-driven photodegradation of plastics. *Nano Lett.* 24, 14082–14090 (2024).
- J. C. Lai, L. Li, D. P. Wang, M. H. Zhang, S.-R. Mo, X. Wang, K. Y. Zeng, C. H. Li, Q. Jiang, X.-Z. You, J.-L. Zuo, A rigid and healable polymer cross-linked by weak but abundant Zn (II)-carboxylate interactions. *Nat. Commun.* 9, 2725 (2018).
- J.-W. Shi, S.-N. Sun, J. Liu, Q. Niu, L.-Z. Dong, Q. Huang, J.-J. Liu, R. Wang, Z. Xin, D. Zhang, J. Niu, Y.-Q. Lan, Calixarene-functionalized stable bismuth oxygen clusters for specific CO₂-to-HCOOH electroreduction. ACS Catal. 12, 14436–14444 (2022).
- J. Rasko, F. Solymosi, Infrared spectroscopic study of the photoinduced activation of CO₂ on TiO₂ and Rh/TiO₂ catalysts. J. Phys. Chem. A 98, 7147–7152 (1994).
- D. D. Miller, S. S. C. Chuang, Control of CO₂ adsorption and desorption using polyethylene glycol in a tetraethylenepentamine thin film: An in situ ATR and theoretical study. *J. Phys. Chem. C* 120, 25489–25504 (2016).
- U. Tumuluri, M. Isenberg, C. S. Tan, S. S. Chuang, In situ infrared study of the effect of amine density on the nature of adsorbed CO₂ on amine-functionalized solid sorbents. *Langmuir* 30, 7405–7413 (2014).
- G. Giubertoni, O. O. Sofronov, H. J. Bakker, Effect of intramolecular hydrogen-bond formation on the molecular conformation of amino acids. Commun. Chem. 3, 84 (2020).
- J. Han, Y. Han, J. Yu, Y. Sun, X. Cui, Q. Ge, J. Sun, Low-temperature CO₂ hydrogenation to olefins on anorthic NaCoFe alloy carbides. *Angew. Chem. Int. Ed. Engl.* 64, e202420621 (2025).
- Y. Pu, H. Zhang, Y. Li, C. Yu, X. Song, C. Yang, M. Fu, Unveiling the role of copper valence states in enhancing the catalytic performance of copper-modified ZSM-5 for direct methane conversion. *Catalysts* 15, 277 (2025).
- S. Li, M. Sun, K. Zhang, X. Cai, Y. Chen, C. Yang, Z. Yang, X. Tang, B. Huang, S. Yang, Covalent elaboration of confined surfaces steers C–C coupling pathway for selective electrochemical CO₂ reduction at ampere-level. *Angew. Chem. Int. Ed. Engl.* 64, e202508366 (2025).
- G. Barany, R. B. Merrifield, A new amino protecting group removable by reduction. Chemistry of the dithiasuccinoyl (Dts) function. J. Am. Chem. Soc. 99, 7363–7365 (1977).
- N. Heidary, K. H. Ly, N. Kornienko, Probing CO₂ conversion chemistry on nanostructured surfaces with operando vibrational spectroscopy. *Nano Lett.* 19, 4817–4826 (2019).
- W. Fang, W. Guo, R. Lu, Y. Yan, X. Liu, D. Wu, F. M. Li, Y. Zhou, C. He, C. Xia, H. Niu, S. Wang, Y. Liu, Y. Mao, C. Zhang, B. You, Y. Pang, L. Duan, X. Yang, F. Song, T. Zhai, G. Wang, X. Guo, B. Tan, T. Yao, Z. Wang, B. Y. Xia, Durable CO₂ conversion in the proton-exchange membrane system. *Nature* 626, 86–91 (2024).
- Y. Maenaka, T. Suenobu, S. Fukuzumi, Catalytic interconversion between hydrogen and formic acid at ambient temperature and pressure. *Energ. Environ. Sci.* 5, 7360–7367 (2012).
- Q. Ge, Y. Liu, K. Li, L. Xie, X. Ruan, W. Wang, L. Wang, T. Wang, W. You, L. Zhang, Significant acceleration of photocatalytic CO₂ reduction at the gas-liquid interface of microdroplets. *Anaew. Chem. Int. Ed. Engl.* 62, e202304189 (2023).
- R. Hudson, R. de Graaf, M. Strandoo Rodin, A. Ohno, N. Lane, S. E. McGlynn, Y. M. A. Yamada, R. Nakamura, L. M. Barge, D. Braun, V. Sojo, CO₂ reduction driven by a pH gradient. *Proc. Natl. Acad. Sci. U.S.A.* 117, 22873–22879 (2020).
- H. Xiong, J. K. Lee, R. N. Zare, W. Min, Strong electric field observed at the interface of aqueous microdroplets. J. Phys. Chem. Lett. 11, 7423–7428 (2020).
- C. R. Baiz, K. J. Kubarych, Ultrafast vibrational stark-effect spectroscopy: Exploring charge-transfer reactions by directly monitoring the solvation shell response. J. Am. Chem. Soc. 132, 12784–12785 (2010).
- X. Zhang, Q. Huang, Y.-X. Liu, J. Yin, S.-F. Pang, P. Liu, Y.-H. Zhang, M. Ge, Microdroplet surface drives and accelerates proton-controlled, size-dependent nitrate photolysis. J. Am. Chem. Soc. 147, 19595–19601 (2025).
- L.-F. Li, P. Liu, Q. Huang, X. Zhang, X. Chao, S. Pang, W. Wang, Y. Cheng, H. Su, Y.-H. Zhang, M. Ge, Rethinking urban haze formation: Atmospheric sulfite conversion rate scales with aerosol surface area, not volume. *One Earth* 7, 1082–1095 (2024).
- X. Fang, Y. Liu, K. Li, T. Wang, Y. Deng, Y. Feng, Y. Yang, H. Cheng, J. Chen, L. Zhang, Atmospheric nitrate formation through oxidation by carbonate radical. ACS Earth Space Chem. 5, 1801–1811 (2021).
- Z. Song, C. Zhu, K. Gong, R. Wang, J. Zhang, S. Zhao, Z. Li, X. Zhang, J. Xie, Deciphering the microdroplet acceleration factors of Aza-Michael addition reactions. *J. Am. Chem. Soc.* 146, 10963–10972 (2024).
- I. Rörig-Dalgaard, Direct measurements of the deliquescence relative humidity in salt mixtures including the contribution from metastable phases. ACS Omega 6, 16297–16306 (2021).

- D. A. Hardy, J. F. Robinson, T. G. Hilditch, E. Neal, P. Lemaitre, J. S. Walker, J. P. Reid, Accurate measurements and simulations of the evaporation and trajectories of individual solution droplets. J. Phys. Chem. B 127, 3416–3430 (2023).
- H. Shi, Z. Cai, J. Patrow, B. Zhao, Y. Wang, Y. Wang, A. Benderskii, J. Dawlaty, S. B. Cronin, Monitoring local electric fields at electrode surfaces using surface enhanced Raman scattering-based Stark-shift spectroscopy during hydrogen evolution reactions. ACS Appl. Mater. Inter. 10, 33678–33683 (2018).
- L. Yang, Y. Liu, Q. Ge, J. Wang, R. Wang, W. You, W. Wang, T. Wang, L. Zhang, Atmospheric hydroxyl radical route revealed: Interface-mediated effects of mineral-bearing microdroplet aerosol. *J. Am. Chem. Soc.* 147, 3371–3382 (2025).
- S. Das, S. Imoto, S. Sun, Y. Nagata, E. H. Backus, M. Bonn, Nature of excess hydrated proton at the water–air interface. J. Am. Chem. Soc. 142, 945–952 (2019).
- K.-H. Huang, Z. Wei, R. G. Cooks, Accelerated reactions of amines with carbon dioxide driven by superacid at the microdroplet interface. Chem. Sci. 12, 2242–2250 (2021).
- P. Saha, S. Amanullah, S. Barman, A. Dey, Electrochemical reduction of CO₂ to CH₃OH catalyzed by an iron porphyrinoid. J. Am. Chem. Soc. 147, 1497–1507 (2025).
- S. Pios, W. Domcke, Reduction of CO₂ with hydrated electrons: Ab initio computational studies for finite-size cluster models. J. Phys. Chem. A 127, 3372–3380 (2023).
- A. Seifitokaldani, C. M. Gabardo, T. Burdyny, C.-T. Dinh, J. P. Edwards, M. G. Kibria,
 O. S. Bushuyev, S. O. Kelley, D. Sinton, E. H. Sargent, Hydronium-induced switching between CO₂ electroreduction pathways. J. Am. Chem. Soc. 140, 3833–3837 (2018).
- P. Xu, X. Ji, M. Li, W. Lu, Small data machine learning in materials science. npj Comput. Mater. 9, 42 (2023).
- 54. Y. Wang, Y. Liu, L. Wang, S. Perumal, H. Wang, H. Ko, C.-L. Dong, P. Zhang, S. Wang, T. T. T. Nga, Y. D. Kim, Y. Ji, S. Zhao, J.-H. Kim, D.-Y. Yee, Y. Hwang, J. Zhang, M. G. Kim, H. Lee, Coupling photocatalytic CO₂ reduction and CH₃OH oxidation for selective dimethoxymethane production. *Nat. Commun.* 15, 6047 (2024).
- S. T. Martin, Phase transitions of aqueous atmospheric particles. Chem. Rev. 100, 3403–3454 (2000).
- J. O. Anhaia-Machado, A. C. G. Soares, C. A. S. de Oliveira Pinto, A. I. Á. Barrera, A. R. Baby,
 G. H. G. Trossini, Molecular modeling based on Time-Dependent Density Functional Theory
 (TD-DFT) applied to the UV-Vis spectra of natural compounds. Chemistry 5, 41–53 (2023).
- C.-L. Xie, J.-M. Xia, R.-Q. Su, J. Li, Y. Liu, X.-W. Yang, Q. Yang, Bacilsubteramide A, a new indole alkaloid, from the deep-sea-derived *Bacillus subterraneus* 11593. *Nat. Prod. Res.* 32, 2553–2557 (2018)
- C. Dayan, E. Fredj, P. K. Misztal, M. Gabay, A. B. Guenther, E. Tas, Emission of biogenic volatile organic compounds from warm and oligotrophic seawater in the Eastern Mediterranean. *Atmos. Chem. Phys.* 20, 12741–12759 (2020).
- H. Petek, J. Zhao, Ultrafast interfacial proton-coupled electron transfer. Chem. Rev. 110, 7082–7099 (2010).
- G. L. Gutsev, R. J. Bartlett, R. N. Compton, Electron affinities of CO₂, OCS, and CS₂. J. Chem. Phys. 108, 6756–6762 (1998).
- H. Qin, H. Zhang, X. Wang, W. Fan, Mechanistic insights into CO₂ hydrogenation to methanol on Cu(110): Unveiling energy linear relationships and enhancing performance strategies. *Phys. Chem. Chem. Phys.* 26, 22739–22751 (2024).
- N. H. Koralegedara, P. X. Pinto, D. D. Dionysiou, S. R. Al-Abed, Recent advances in flue gas desulfurization gypsum processes and applications – A review. J. Environ. Manage. 251, 109572 (2019)
- 63. H.-C. Chang, K.-H. Huang, Y.-L. Yeh, S. H. Lin, A high-pressure FT-IR study of the isotope effects on water and high-pressure ices. *Chem. Phys. Lett.* **326**, 93–100 (2000).
- 64. Y. Yang, G. Wang, M. Zhou, Infrared spectroscopy of [M (CO₂)_n]⁺ (M = Ca, Sr, and Ba; n = 1–4) in the gas phase: Solvation-induced electron transfer and activation of CO₂. J. Phys. Chem. A 128, 618–625 (2024).
- X. Cui, H. Bai, J. Zhang, R. Liu, H. Yu, Y. Wang, T. Kong, M.-Y. Gao, Z. Lu, Y. Xiong, A cluster-nanozyme-coenzyme system mimicking natural photosynthesis for CO₂ reduction under intermittent light irradiation. *Nat. Commun.* 15, 9048 (2024).
- P. Wang, X. Ba, X. Zhang, H. Gao, M. Han, Z. Zhao, X. Chen, L. Wang, X. Diao, G. Wang, Direct Z-scheme heterojunction of PCN-222/CsPbBr₃ for boosting photocatalytic CO₂ reduction to HCOOH. Chem. Eng. J. 457, 141248 (2023).
- H. Wang, S. Cheng, X. Cai, L. Cheng, R. Zhou, T. Hou, Y. Li, Photocatalytic CO₂ reduction to HCOOH over core-shell Cu@Cu₂O catalysts. Catal. Commun 162, 106372 (2022).
- X. Wang, J. Li, M. Kou, W. Dou, D. Bai, X. Tang, Y. Tang, W. Liu, Dual-function preciousmetal-free metal-organic framework for photocatalytic conversion and chemical fixation of carbon dioxide. *Inorg. Chem.* 62, 19015–19024 (2023).
- Y.-N. Gong, W. Zhong, Y. Li, Y. Qiu, L. Zheng, J. Jiang, H.-L. Jiang, Regulating photocatalysis by spin-state manipulation of cobalt in covalent organic frameworks. *J. Am. Chem. Soc.* 142, 16723–16731 (2020).
- M. Ma, Z. Huang, R. Wang, R. Zhang, T. Yang, Z. Rao, W. Fa, F. Zhang, Y. Cao, S. Yu, Y. Zhou, Targeted H₂O activation to manipulate the selective photocatalytic reduction of CO₂ to CH₃OH over carbon nitride-supported cobalt sulfide. *Green Chem.* 24, 8791–8799 (2022).

SCIENCE ADVANCES | RESEARCH ARTICLE

- D. O. Adekoya, M. Tahir, N. A. S. Amin, g-C₃N₄/(Cu/TiO₂) nanocomposite for enhanced photoreduction of CO₂ to CH₃OH and HCOOH under UV/visible light. *J. CO2 Util.* 18, 261–274 (2017).
- F. Xu, J. Zhang, B. Zhu, J. Yu, J. Xu, CulnS₂ sensitized TiO₂ hybrid nanofibers for improved photocatalytic CO₂ reduction. *Appl. Catal. B Environ.* 230, 194–202 (2018).
- C. An, J. Wang, W. Jiang, M. Zhang, X. Ming, S. Wang, Q. Zhang, Strongly visible-light responsive plasmonic shaped AgX: Ag (X= CI, Br) nanoparticles for reduction of CO₂ to methanol. *Nanoscale* 4, 5646–5650 (2012).
- M. A. Gondal, M. A. Dastageer, L. E. Oloore, U. Baig, Laser induced selective photocatalytic reduction of CO₂ into methanol using In₂O₃-WO₃ nano-composite. *J. Photoch. Photo. A* 343, 40–50 (2017).
- R. Wang, M. Zhang, S. Zhang, J. Zheng, Y. Zeng, Y. Yang, J. Ding, X. Wu, Q. Zhong, Selfsupporting triphase photocatalytic CO₂ reduction to CH₃OH on controllable core–shell structure with tunable interfacial wettability. ACS Nano 17, 24363–24373 (2023).
- J. Zhou, J. Li, L. Kan, L. Zhang, Q. Huang, Y. Yan, Y. Chen, J. Liu, S.-L. Li, Y.-Q. Lan, Linking oxidative and reductive clusters to prepare crystalline porous catalysts for photocatalytic CO₂ reduction with H₂O. *Nat. Commun.* 13, 4681 (2022).
- 77. Y.-C. Hao, L.-W. Chen, J. Li, Y. Guo, X. Su, M. Shu, Q. Zhang, W.-Y. Gao, S. Li, Z.-L. Yu, L. Gu, X. Feng, A.-X. Yin, R. Si, Y.-W. Zhang, B. Wang, C.-H. Yan, Metal-organic framework

membranes with single-atomic centers for photocatalytic CO₂ and O₂ reduction. *Nat. Commun.* **12**, 2682 (2021).

Acknowledgments: We thank all colleagues and collaborators for valuable support and insightful discussions. Funding: This work was supported by the National Natural Science Foundation of China (no. 22376028, to L.Z.; no. 22176036, to L.Z.; no. 62425501, to M.J.; no. 22382601, to Q.G.) and Natural Science Foundation of Shanghai (no. 19ZR1471200, to L.Z.).

Author contributions: Conceptualization: Q.G., Y.L., and L.Z. Methodology: Q.G. and Y.L. Investigation: Q.G., Y.L., W.Y., W.W., L.X., M.M., L.Y., K.L., X.R., L.W., J.W., R.W., T.W., T.H., and M.J. Visualization: Q.G., Y.L., w.W., and W.Y. Supervision: Q.G., Y.L., and L.Z. Writing—original draft: Q.G. Writing—review and editing: Q.G., Y.L., and L.Z. Competing interests: The authors declare they have no competing interests. Data and materials availability: All data needed to evaluate the conclusions in the paper are present in the paper and/or the Supplementary Materials.

Submitted 2 April 2025 Accepted 9 September 2025 Published 8 October 2025 10.1126/sciadv.adx5714